

Mechanical state, material properties and continuous description of an epithelial tissue

Isabelle Bonnet¹, Philippe Marcq², Floris Bosveld¹, Luc Fetler², Yohanns Bellaïche^{1,*} and François Graner^{1,†}

¹ *Genetics and Developmental Biology,
Team ‘Polarity, division and morphogenesis’,
Institut Curie, UMR3215 CNRS, U934 Inserm, UPMC*

² *Physico-Chimie Curie, Institut Curie,
UMR168 CNRS, UPMC
26 rue d’Ulm, F-75248 Paris Cedex 05 France*

(Dated: May 8, 2012)

During development, epithelial tissues undergo extensive morphogenesis based on coordinated changes of cell shape and position over time. Continuum mechanics describes tissue mechanical state and shape changes in terms of strain and stress. It accounts for individual cell properties using only a few spatially averaged material parameters. To determine the mechanical state and parameters in the *Drosophila* pupa dorsal thorax epithelium, we sever *in vivo* the adherens junctions around a disk-shaped domain comprising typically hundred cells. This enables a direct measurement of the strain along different orientations at once. The amplitude and anisotropy of the strain increase during development. We also measure the stress to viscosity ratio and similarly find an increase in amplitude and anisotropy. The relaxation time is of order of ten seconds. We propose a space-time, continuous model of the relaxation. Good agreement with experimental data validates the description of the epithelial domain as a continuous, linear, visco-elastic material. We discuss the relevant time and length scales. Another material parameter, the ratio of external friction to internal viscosity, is estimated by fitting the initial velocity profile. Together, our results contribute to quantify forces and displacements, and their time evolution during morphogenesis.

Keywords: Epithelial tissue, continuum mechanics, laser severing, *Drosophila* development, live imaging

I. INTRODUCTION

An epithelial tissue is a sheet of cells that acts as a barrier, separating for instance the outside and the inside of a multicellular organism. Its biological function relies in part on the formation of a network of adherens junction belts, connected to the acto-myosin cytoskeleton, where cells adhere to each other [1], and which transmits mechanical information over several cell diameters [1–3]. A key issue is to understand and model the role of tissue mechanics (forces, displacements, and their time evolution) in the coordinated changes of cell shape and position which determine morphogenetic flows at the tissue level [1, 4, 5].

Several models describe tissues using *continuum mechanics* [3, 6–12]. One precondition is the existence of a mesoscopic scale defining a domain over which averages of cell properties are well-defined [6, 13]. This description further relies on the assumption that the tissue mechanical state can be quantified, at the same mesoscopic scale, by two variables [6]: the stress characterizing in which directions, and to what extent, the domain is under tension or under compression; and the strain characterizing how far the domain geometry is from that of a relaxed state. Such description has the advantage of accounting for individual cell properties using only a few spatially averaged parameters, which determine for instance how

fast and through which succession of states the domain reacts to external solicitations.

Beyond simple observation, *in vivo* mechanical measurement techniques include elastography [14], photoelasticity [15], magnetic micromanipulation [16], tonometry [17] or nanoindentation [18]. A large literature (for review, see *e.g.* [19]) has established laser ablation of individual cell junctions as a tool to measure the tensions within an epithelium, in particular during *Drosophila* dorsal closure [3, 20–24]. This technique has allowed to measure the material relaxation time τ and contributed to a better characterization of morphogenetic processes in *Drosophila* [25–28].

The analysis of single cell junction ablation is usually based on reasonable assumptions [19, 20]: that the tissue is at mechanical equilibrium just before severing; that the ablation is effective in removing at least part of the cell junction tension; and that during relaxation the velocity remains small (Reynolds number much smaller than 1). Within these assumptions, the initial retraction velocity yields the value of the cell junction tension removed by the ablation, up to an unknown prefactor which depends on the dissipation [25–29].

The tensor σ denotes the component of the stress removed by ablation. It arises as an average over several individual cell junctions within a region of the tissue. By ablating straight lines in either of two perpendicular directions [30, 31] or by performing statistics on single cell junction ablations in several directions [3], it is possible to measure step by step the anisotropy of the ratio σ/η (where η denotes the tissue viscosity). The stress to viscosity ratio σ/η is the initial strain rate after the

* yohanns.bellaiche@curie.fr

† francois.graner@curie.fr

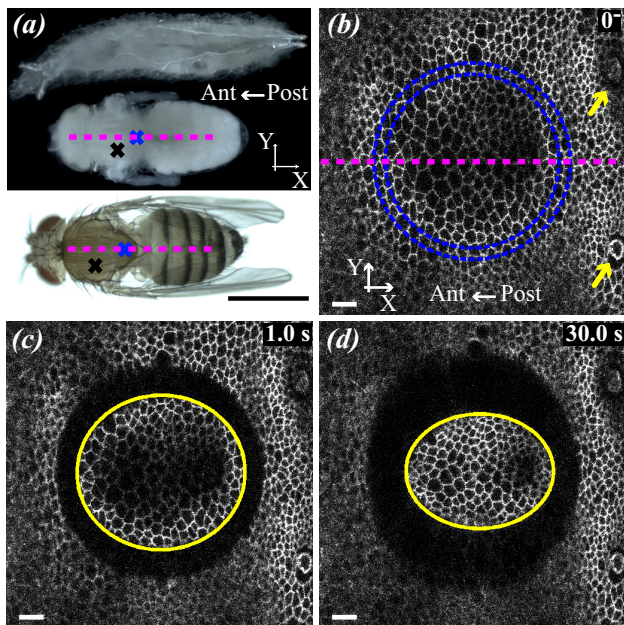


FIG. 1. Large-size annular severing in a fly dorsal thorax. (a) Developmental stages of a fruit fly *Drosophila melanogaster*. Top: larva. Middle: pupa, with pupal case removed (ESM Figure 1) and cuticle kept intact. Bottom: adult. Dashed lines represent the midline (symmetry axis). The X axis is antero-posterior: anterior (head) towards the left, posterior (abdomen) towards the right. The Y axis is medio-lateral. Crosses: approximate positions of severing, along the midline in the scutellum (blue) and off-axis in the scutum (black). (b) Epithelial cell apical junctions marked by E-Cadherin:GFP just before the severing, $t = 0^-$, here in an old pupa (see text for classification). Blue circles: two concentric circles define the annular severed region; the distance between circles corresponds to about one cell size. Yellow arrows: macrochaete used as spatial references to position the severed region. (c) First image after severing, $t = 1$ s. Yellow: fitted ellipse [36] (see Methods). (d) Time $t = 30$ s after the severing, showing a larger opening along Y than X . Bars = 1 mm (a), 10 μm (b-d).

severing: the rate of displacement that the epithelium would spontaneously undergo if it were free.

The continuous description applies to other cellular materials such as foams [32, 33]. In the present work, we investigate experimentally whether it also applies to epithelial tissues. More specifically, we ask whether the epithelium strain, stress and material properties can be directly measured on a mesoscopic scale.

We address these questions in a model system, the dorsal thorax epithelium of *Drosophila* pupa. The pupa is the life stage during which the larva starves, feeds upon its reserves and metamorphoses into an adult [34]. The dorsal thorax is a single layer of cells whose apical surfaces, surrounded by the adherens junction belts, face the cuticle, which protects the pupa; their basal surfaces face

the hemolymph, which acts as a nutrient transporter. It is composed of a large anterior region, the scutum, and a posterior tip, the scutellum. The thorax, and especially the scutellum, undergoes extensive morphogenetic changes during the metamorphosis that shapes the adult fly (Figure 1 (a)), making it a useful model to decipher the mechanisms that control tissue morphogenesis during development [29]. It has a bilateral symmetry axis: the midline (axis X , dashed line in Figure 1 (a-b)). It displays large cells, the macrochaete (precursor cells of adult sensory hairs, Figure 1 (b)), whose positions are precisely reproducible [35].

II. ANNULAR SEVERING EXPERIMENTS

We introduce an original type of severing experiment. We sever by short pulse laser the adherens junctions in an annular region around a ~ 30 μm radius circular tissue domain (see Figure 1 (b-d), Methods and Movies 1-3). The inner and outer wound margins display a comparable speed, displacement and anisotropy. Note that the same anisotropy in speed and displacement results in the outer ellipse boundary having minor and major axes orthogonal to the minor and major axes of the inner one. After severing, the wound heals within tens of minutes and the pupa develops to adult.

Experiments are done in the scutellum (blue cross in Figure 1 (a)). We classify them into three groups, according to the developmental age at which the severing is performed: earlier than 15-16 h, approximately 18-20 h, and later than 24-26 h after pupa formation. For brevity we call them “young” ($N = 8$), “middle-aged” ($N = 5$) and “old” ($N = 10$) pupae, respectively. Similar experiments can be performed in other locations. As a proof of principle, we include three experiments performed in the scutum (black cross in Figure 1 (a)) of middle-aged ($N = 2$) and old ($N = 1$) pupae.

We analyse the retraction of the inner tissue domain and its margin, within the set of assumptions relevant for the retraction of a single severed cell-junction. The boundary of the retracting domain is fitted at each time point by an ellipse [36] (see Methods and Figure 1 (c-d)), yielding values of the X and Y axes as a function of time (Figure 2).

Our protocol offers several advantages. (i) The experiment directly yields measurements averaged over the severed tissue domain, comprising typically a hundred of cells. As discussed below, the domain size is thus an adequate mesoscopic scale, crossing-over from detailed cell-level to tissue-level continuous descriptions [6, 13]. (ii) The comparison between the initial and final states yields a direct measurement of the strain which existed before severing. (iii) Several cell-cell junctions in various directions are severed at once (rather than step by step) and in the same pupa. Hence one experiment yields a direct measurement of all stress to viscosity tensor components. It takes only a few tens of seconds, the typical value of

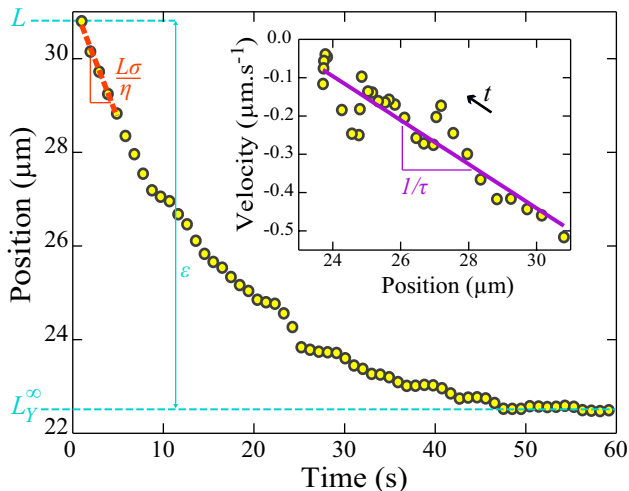


FIG. 2. Model-independent measurement of strain ε , stress to viscosity ratio σ/η , and relaxation time τ . The wound margin position (ellipse semi-axis) is plotted *versus* time after severing; data from Figure 1 (b-d), ESM Movie 1, along the Y axis. The difference between the initial (L) and final (L_Y^∞) positions (blue dashed lines) directly yields the value of $\varepsilon = \ln(L/L_Y^\infty)$. The initial velocity $-\frac{dY}{dt}(t=0)$ (slope of the orange dashed line) yields an estimate of $L\sigma/\eta$. Inset: Velocity, estimated by finite differences of successive positions, *versus* the position during the first 30 s. An arrow indicates the direction of increasing time t . The slope of a linear fit (purple line) yields the inverse of the relaxation time, $1/\tau$ (see Equation 2).

the relaxation time. (iv) Last but not least, by isolating in time and space an epithelium domain from its neighboring cells, we obtain a complete set of well-defined initial, boundary and final conditions for a spatio-temporal model of the retracting domain. We thus introduce a continuous model, in the spirit of Mayer *et al.* [30] and taking into account a coupling between space and time dependences. As explained below, fitting such a model to the displacements in the domain bulk tests the continuous description, suggests an interpretation of the relaxation time, and probes the competition between internal viscosity and external friction.

III. RESULTS

A. Model-independent measurement of strain, stress to viscosity ratio and relaxation time

Severing the epithelium reveals the displacement that the epithelium would spontaneously undergo if it were free. We measure the strain using a logarithmic definition [32, 37, 38], Hencky’s “true strain” [39]:

$$\varepsilon_{XX} = \int_{L_X^\infty}^L \frac{dX}{X} = \ln\left(\frac{L}{L_X^\infty}\right), \quad (1)$$

where L is the initial radius, and L_X^∞ is the ellipse semi-axis at the end of the relaxation. Similarly $\varepsilon_{YY} =$

$\ln(L/L_Y^\infty)$. The advantages of this definition are that [32, 33]: it is valid at all amplitudes; it is adapted for tensorial measurements; and finally it increases the range of validity of the linear elasticity approximation which applies here even to the highest strain value we measure, 0.45.

Each severing is followed by a relaxation to a final domain strictly smaller than the initial disk (Figure 1 (d)), indicating that before the severing the tissue had a positive strain in all directions. Since the midline is a symmetry axis, we expect that the strain axes are parallel and perpendicular to it. We check that this is the case for the fitted ellipse axes, and that accordingly the shear strain ε_{XY} is indistinguishable from 0. We thus plot ε_{XX} and ε_{YY} (Figure 3 (a)), obtained with absolute precision better than 10^{-2} . The values are clustered according to the three pupa age groups: ε is low and isotropic at young age (green cluster), moderate and isotropic at middle age (red), high and anisotropic ($\varepsilon_{YY} > \varepsilon_{XX}$) at old age (blue).

Similarly, in each experiment, the initial retraction of the wound margins (Figure 1 (c)) indicates the sign of the stress: before the severing the tissue was under tensile stress in all directions. This is reminiscent of positive cell junction tensions observed in the wing [25] and in the notum [29]. The initial retraction velocity divided by L yields the stress to viscosity ratio σ/η (Figure 2), in a way which is likely to be independent of any tissue rheological model, as suggested by the following argument. When ablating a single cell-cell junction, force balance shows that the force F exerted by the ablated junction on the neighbouring vertex is proportional to the initial recoil velocity v : $F = -\gamma v$, where γ is a friction coefficient [19]. Coarse-graining this relation, and assuming that the main source of dissipation is identical in our experiments which sever many junctions at once, yields $\sigma \sim \eta v/L$, where the factor L is introduced by dimensional analysis. Results for the stress to viscosity ratio σ/η (Figure 3 (b)) are similar to those for ε : its amplitude and anisotropy are initially small and increase with age; the values are clustered according to the three age groups; no shear stress is detected. Values of σ/η span almost two decades, reflecting the sensitivity and precision of the method.

The relaxation time, τ , is obtained from the time evolution of the ellipse axes. Instead of fitting an exponential to the data, we plot the velocity *versus* position (Inset of Figure 2). This method is robust and independent of any assumption. A linear regression of the velocity as a function of position yields a slope of $-1/\tau$, as seen, *e.g.*, in the equation:

$$\frac{dY}{dt}(t) = -\frac{Y(t) - L_Y^\infty}{\tau_Y}. \quad (2)$$

We find that the relaxation time is approximately isotropic (ESM Figure 3 (A)) and use $(\tau_X + \tau_Y)/2$ as an estimate of τ . It is close to 10 s and only slightly varies with the pupa age group (Figure 3 (c), vertical axis).

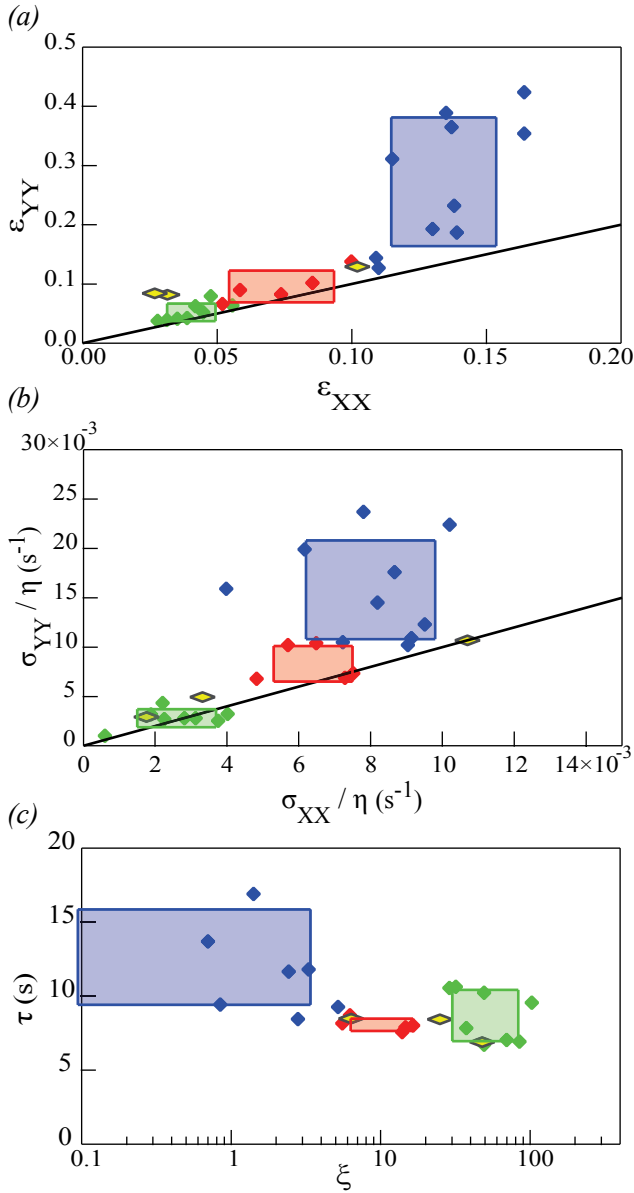


FIG. 3. Mechanical state and material properties. Color code according to pupa development ages: green, young; red, middle-aged; blue, old. The edges of the rectangular regions represent the mean values \pm standard deviations for each group. The experiments in the scutum are in yellow. (a) Strain anisotropy: ε_{YY} versus ε_{XX} . Note the difference in horizontal and vertical scales; the solid line is the first bisectrix $Y = X$, indicating the reference for isotropy. (b) Same for the severed stress to viscosity ratio σ/η . (c) Relaxation time τ and dimensionless friction to viscosity ratio ξ ; values are the averages of the measurements along the X and Y axes (ESM Figure 3). Note the semi-log scale. The blue rectangle takes into account two very small values of ξ , of order 10^{-3} and 10^{-4} (below the plotted range).

B. Space-time model and measurement of the friction to viscosity ratio

To describe the bulk of the retracting domain, we track the displacements of around a hundred features in a band of tissue (Figure 4 and Methods). Spatially averaging their positions by binning them into 8 equal-size bins improves the signal to noise ratio. We obtain the initial velocity profile *versus* position (Figure 5). For old pupae, it is spatially linear; for middle-aged pupae it is spatially nonlinear; in the young pupae, immediately after severing only the boundaries move significantly.

To account for these observations, we formulate a spatio-temporal, viscoelastic, Kelvin-Voigt model in one dimension of space, where the coordinate z denotes either X or Y , and t denotes time after severing (see ESM). Thanks to the definition (1), the strain $\varepsilon(z, t)$ is related without approximation to the velocity $v(z, t)$ through:

$$\frac{\partial v}{\partial z} = \frac{\partial \varepsilon}{\partial t}, \quad (3)$$

We model the effect of friction of the epithelium against the hemolymph and the cuticle as an external fluid friction with coefficient ζ . We find that when internal viscosity dominates, the strain remains uniform and all parts of the tissue relax exponentially with the same viscoelastic relaxation time $\tau = \eta/E$ where E is the Young modulus (ESM Figure 4 (A)). When external friction dominates, strain diffuses from the boundaries with a diffusion coefficient $D = E/\zeta$ and remains thus inhomogeneous at times t smaller than $\tau_D = L^2/D = \zeta L^2/E$ (ESM Figure 4 (B)). In the general case, the dynamical equation for the strain field $\varepsilon(z, t)$ reads:

$$\frac{\partial \varepsilon}{\partial t} = D \frac{\partial^2}{\partial z^2} \left(\varepsilon + \tau \frac{\partial \varepsilon}{\partial t} \right), \quad (4)$$

with the conditions $\varepsilon(z, t = 0) = \varepsilon_0$ initially, $\varepsilon(z = \pm L, t) = \varepsilon_0 \exp(-t/\tau)$ at boundaries, and $\varepsilon(z, t \rightarrow \infty) = 0$ at the end. The relative importance of external friction *versus* internal viscosity is quantified by the dimensionless parameter:

$$\xi = \frac{\zeta L^2}{\eta} = \frac{\tau_D}{\tau}. \quad (5)$$

Solving Equation 4 at short time and integrating over space Equation 3 at $t = 0$ yields the initial velocity profile:

$$v(z, t = 0) = -\varepsilon_0 \frac{L}{\tau} \frac{1}{\xi^{1/2} \cosh \xi^{1/2}} \sinh \left(\xi^{1/2} \frac{z}{L} \right), \quad (6)$$

whose curvature is controlled by ξ . We thus estimate ξ by fitting a hyperbolic sine to experimental initial velocity profiles (Figure 5). As for the relaxation time, we check that the values ξ_X and ξ_Y determined in the directions X and Y are roughly consistent (ESM Figure 3 (B)): we thus use $(\xi_X + \xi_Y)/2$ as an estimate of ξ .

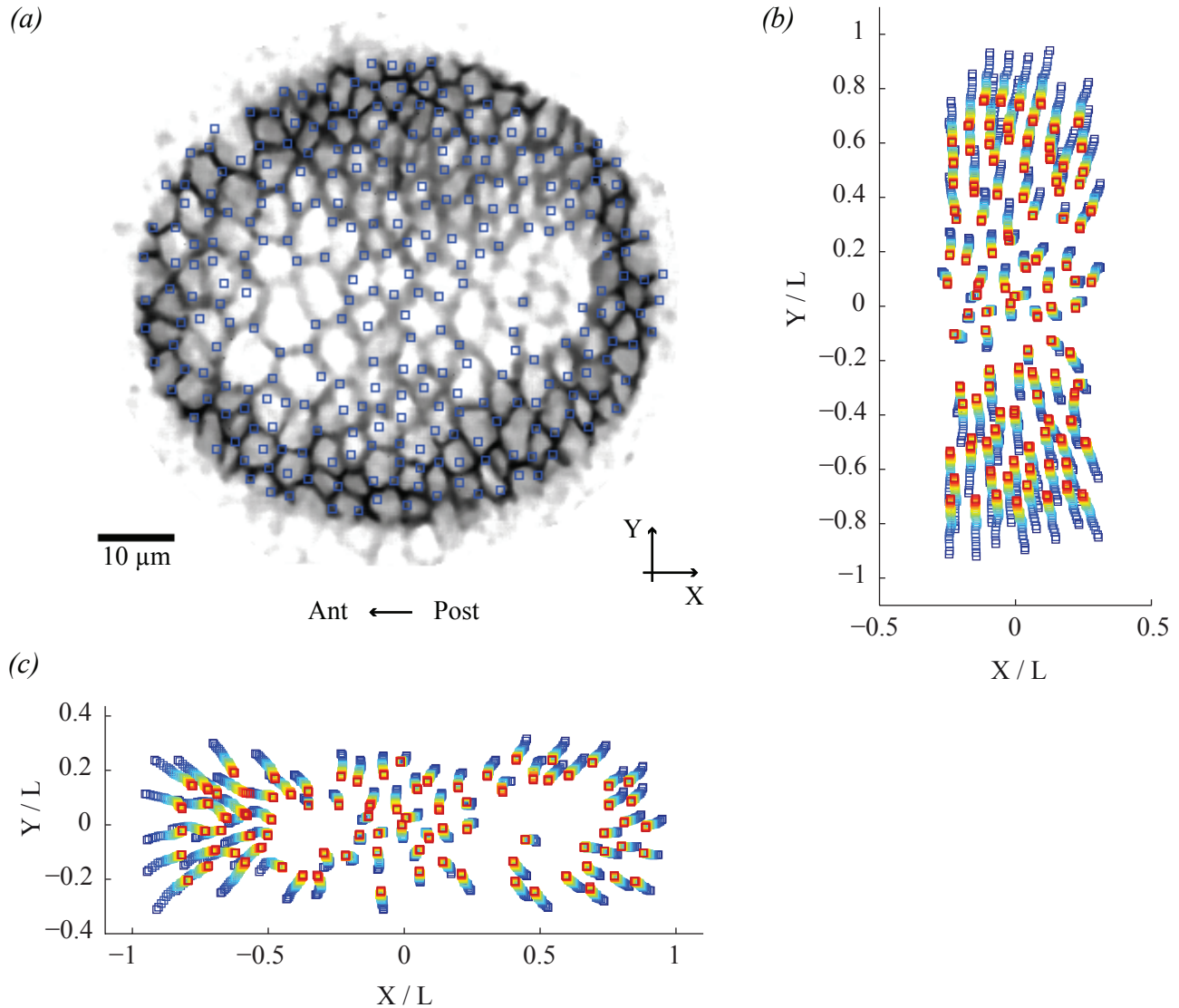


FIG. 4. Tracking of feature positions. (a) Positions of features (blue squares), old pupa, data of Figure 1 (c) after image denoising. The logarithms of intensity levels are represented in grey scale, and contrast is inverted for clarity. (b) Tracking for the first 30 s (time color-coded from blue to red), inside a rectangle along the Y axis. (c) Same for the X axis.

We find that ξ varies more than τ (Figure 3 (c), horizontal axis). The middle aged group is characterized by intermediate values of ξ (Figure 5, red), of order of 10. According to Equation 5, this indicates a possible effect of the external friction on the relaxation for scales larger than $L/\sqrt{\xi} \sim 10 \mu\text{m}$. For both other age groups, the values of ξ should be considered as bounds on the order of magnitude. For old pupae we find ξ smaller than a few times unity (Figure 5, blue). For young pupae, we find ξ larger than a few tens or hundred (Figure 5, green).

This model depends on three parameters measured independently of each other: the initial strain ε_0 , the viscoelastic time τ , and the friction to viscosity ratio ξ . To validate the model, we use it to numerically compute the

whole space-time map of strains and displacements. We simulate each experiment using the values of τ and ξ measured as described above. Figure 6 shows that we find a good agreement with experimental data. Moreover, we plot the square deviation between experimental and numerical data as a function of the parameter values (τ, ξ) (see Methods). We check that the error landscapes we obtain are broadly consistent with our experimental estimates of ξ and τ (ESM Figure 5).

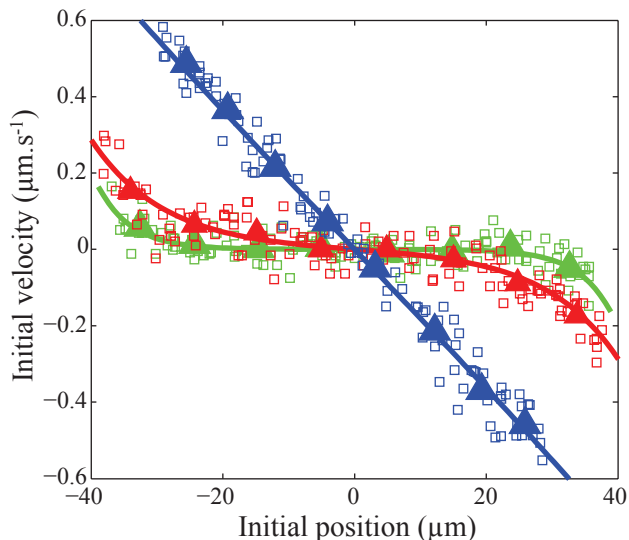


FIG. 5. Model-dependent measurement of the friction to viscosity ratio ξ . Initial velocity profiles immediately after severing are plotted *versus* initial position prior to severing, for three typical pupae: young (green), middle-aged (red) and old (blue). Open squares: features, from Figure 4 (b). Closed triangles: same, spatially averaged in 8 bins. Lines: fit by a sinh function (Equation 6), yielding for ξ a value either above, in, or below the measurable range: $\xi > 60$ (green), $\xi \sim 14 \pm 5$ (red), $\xi < 0.5$ (blue), respectively.

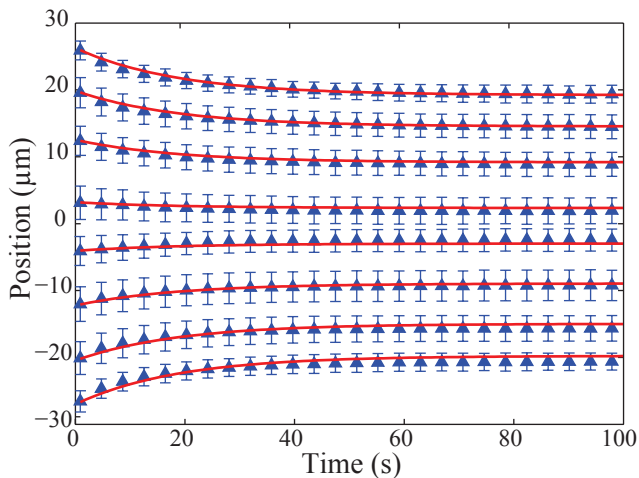


FIG. 6. Validation of the model. Blue triangles: positions of features from Figure 4 (b), spatially averaged in bins *versus* time after severing; bars: standard deviation. Red lines: numerical resolution of Equation 3, using the measured values $\xi = 0.08$, $\tau = 15.8$ s.

IV. DISCUSSION

A. Time scale

We report relaxation times τ in the range 5 to 20 s, and initial velocities in the range 0.1 to 0.6 $\mu\text{m}\cdot\text{s}^{-1}$. This

agrees with values provided by single cell junction ablation: 10-100 s for the relaxation times, 0.1 to 1 $\mu\text{m}\cdot\text{s}^{-1}$ for the initial velocities in other *Drosophila* tissues [3, 25–28]. The model allows to interpret τ as a viscoelastic time. Its order of magnitude is typical of the viscoelastic times corresponding to cell *internal* degrees of freedom [40], also measured in cell aggregates [41, 42].

Conversely *external* degrees of freedom (such as cell-cell rearrangements or cell divisions) would have much larger viscoelastic times: in cell aggregates they are typically of order of several hours [11, 41, 43]. The time scales of morphogenesis in this tissue are also of order of hours [29], as observed in other tissues as well, such as the *Drosophila* pupal wing [12]. Indeed continuous models of morphogenetic processes presuppose the existence of such a separation of time scales.

The present experimental data are well described assuming that a single viscoelastic time is relevant. Other experiments display a wide distribution of viscoelastic times [3, 28]: the model can easily be modified so as to take this feature into account. Note that in the presence of friction the model already predicts that different parts of the severed domain relax at different rates (ESM Figure 4 (B)).

B. Length scale

Measurements of ε , σ/η , τ and ξ are performed as averages over the severed disk. The requirements on the averaging scale are that it should be (i) large enough to obtain a sufficient signal to noise ratio yielding significant results, and (ii) small enough to be able to focus simultaneously on the whole severed ring despite the epithelium surface curvature which is observed in old pupae. The $Y \rightarrow -Y$ symmetry with respect to the midline observed in Figures 1 (b-d), 5, and 6 acts as a control of the signal to noise ratio. The experimentally available range of scales corresponds to 60-100 cell areas, in other words the semi-axis length L corresponds to 4-5 cell diameters. For old pupae, scales smaller than L are also probed, corresponding to the scale of bins (at least $L/2$ or $L/4$, see Figs. 5 and 6).

C. Friction

We experimentally determine the order of magnitude of the dimensionless friction to viscosity ratio, ξ (Figure 3 (c), horizontal axis). Obtaining more precise values of ξ would depend on model ingredients, such as depth of ablation along the apico-basal axis, detailed cell geometry, tissue compressibility, or type of friction.

For simplicity we have modeled by a fluid friction [30] the dissipation on either surfaces of the epithelium, namely the hemolymph at basal side and the cuticle at apical side. We do not observe any threshold effect due

to solid friction, and the agreement between model and data justifies *a posteriori* our assumption.

For young pupae, the initial velocity field is not significantly higher than the noise level (Figure 5, green). In this age group, it cannot be used to validate the model, and the estimate of ξ strongly depends on the motion of domain parts located close to the boundary (Equation 6).

D. Continuous description

In the dorsal thorax, the severed domain fulfills the theoretical requirements for a continuous description: it contains a number of cells much larger than one (large enough to allow for averaging), while being much smaller than the total number of cells in the whole tissue.

One could ask whether averages at scale L are meaningful, due to variation of cell properties from cell to cell. We speculate that if heterogeneities within the domain dominated the average, the domain boundary could in principle adopt any arbitrary shape compatible with the $Y \rightarrow -Y$ symmetry. However, in practice, we observe that the domain boundary at the beginning, as well as at the end, of the relaxation also displays a $X \rightarrow -X$ symmetry (Figure 1 (b-d) and Movies 1-3) and can be fitted by an ellipse: this is consistent with the measurements of σ/η and ε as tensors averaged over scale L .

E. Model

Limits of our model lie in its simplifications: one dimensional treatment, linear elasticity and viscosity, isotropy and homogeneity of material parameters including friction, identical properties of all cells contained in the severed region. However, the agreement between model and experiment is already good, and validates these approximations *a posteriori*. We emphasize that one major goal of this model is to provide an order of magnitude of the friction to viscosity ratio ξ . We do not claim that this model is unique, nor that it is general. In the future we hope to further test the model ingredients and relevance on this epithelium and other quasi-planar ones.

Since its ingredients are general, we expect our model to be of broad relevance when studying the relaxation of quasi-planar epithelia over similar time and length scales. However, the simplifications involved deserve further comments. In fact, completely different hypotheses could also be invoked to explain the spatial non-linearity in the velocity profile observed for young and middle-aged pupae. For instance, the viscous component of biological tissues could be a non-linear function of time, strain, and strain rate [6]. A strain-dependent viscosity coefficient may lead to a non-linear velocity profile without the need to invoke any external friction. Alternatively, a spatially heterogeneous friction might also explain the observed velocity profiles. Since a linear velocity profile

is observed in older pupae, the amplitude of these additional, more complex ingredients would have to decrease strongly during development.

We believe that our model has the merit of simplicity. It successfully accounts for the description of the velocity profiles at any time. Each of its hypotheses could be tested experimentally and, if experimental results require it, hypotheses could be relaxed to lead to more detailed explorations. We expect that additional ingredients could strongly affect the value of ξ , but that other measurements presented here (namely ε , σ/η and τ) should be robust. The model thus provides a flexible and robust route to a mechanical description of quasi-planar epithelia.

F. Perspectives

Building upon classical single-junction laser ablations, our experiments enable to measure the time evolution of the mechanical state (strain, and stress to viscosity ratio) and material properties (relaxation time, and friction to viscosity ratio) during pupa metamorphosis, as well as their anisotropy. This provides relevant ingredients for the modeling of a tissue as a continuous, linear, viscoelastic material.

Moreover, our approach provides a method to explore the biological causality of the observed properties, by analysing mutant phenotypes or by micro-injecting drugs. We conjecture that τ would be affected by low doses of drugs known to modify cytoskeletal rheology such as Cytochalasin D [44], CK-666 [45], Y-27632 [46] which respectively inhibit actin polymerization, Arp2/3 complex activity or Rho-Kinase activity. We anticipate that modulating cell-cell adhesion by knock-down of E-Cadherin or Catenins [47] could affect the viscosity. Although we cannot modulate the cell-cuticle adhesion, we could tune cell-matrix adhesion by knock-down of integrin or its linker to the cytoskeleton [47] to affect the friction and thereby modify ξ .

In principle, by establishing a complete map of σ at different positions, one could determine the length scale at which σ varies within the tissue, and check *a posteriori* whether it is larger than the scale L used to measure σ . However, the present experiments measure the stress up to a dissipative prefactor, the tissue viscosity. Similarly, single cell-junction ablation experiments measure force up to a prefactor (a friction coefficient), rarely discussed or measured in the literature. To separate the stress and viscosity variations, alternative methods to directly measure forces and viscosities in live epithelia are thus called for. These include the measurement of cell junction tensions from movies observations [48], where the unknown prefactor, namely the average tension over the whole image, is by definition the same for all junctions. External mechanical manipulation [16–18] yields direct determination of out-of-plane elastic and/or viscous moduli, but the in-plane moduli are only indirectly determined. An-

other possible strategy could rely on microrheology [49–51]: either passive, by tracking the brownian diffusion of beads within the cells; or active, by moving (magnetically or optically) a bead back and forth within a cell at a specified frequency. Such measurements could yield a direct access to the value of η , but at the intracellular level. Measuring η at the scale of several cells either directly, or indirectly by measuring E and τ and using the relation $\eta = E\tau$, could probably be possible, but we are not aware yet of a published method.

Since ε is a dimensionless geometrical quantity, its value is insensitive to cell size: the observed ~ 7 -fold increase in ε cannot be related to changes of cell size over time. It should involve other causes, that remain to be determined. Part of the measured increase in σ/η values may be due to cell divisions which decrease the average cell area by a factor of ~ 2 between young and old pupae. The observed increase is a factor of ~ 25 , and thus should involve other causes as well. One candidate is a decrease of the tissue viscosity η . However the near constancy of the viscoelastic time would then imply a corresponding increase in tissue elasticity, a rather unlikely coincidence. We therefore expect that stronger tensile forces are at work in the tissue in older pupae. From 18 hours APF onwards, the lateral part of the scutellum undergoes apical cell contractions that shape the lateral domain of the tissue [29]. This observation led us to divide the ablation experiments into the three age groups. It may also explain the changes in mechanical properties measured in the tissue for middle-aged and old pupae. To precisely analyse the causes of the increases in ε and σ/η would therefore require to identify genes that specifically affect the lateral contraction of the tissue.

Our experimental method should be applicable to other tissues. Performing experiments in an epithelium which is flat enough to significantly increase L , and with a sufficient signal to noise ratio on the estimate of ξ , would enable to check the scaling of ξ *versus* L given by Equation 5.

V. METHODS

A. Experiments

Drosophila melanogaster larvae were collected at the beginning of metamorphosis (pupa formation) [52]. The pupae were kept at 25°C, then dissected and mounted as described in [53] (ESM Figure 1). Using the adherens junction protein E-Cadherin fused to Green Fluorescent Protein [54] we imaged the apical cell junctions by fluorescent microscopy [53].

The time-lapse laser-scanning microscope LSM710 NLO (Carl Zeiss MicroImaging) collected 512×512 pixel images in mono-photon mode at 488 nm excitation (pixel size in the range 0.24 to 0.29 μm) through a Plan-Apochromat 63×1.40 oil objective. Before and after severing, the time interval between two consecutive frames

was either 393 ms or 970 ms according to the scanning mode (bi- or mono-directional), without any apparent effect on the results presented here. We focused on the adherens junctions to be severed; due to the epithelial surface curvature especially in old pupae, adherens junctions of innermost and outermost regions were slightly out of focus (Figure 1 and Movies 1-3).

We defined a region of interest as an annular region between two concentric circles. We severed it at the 10th frame (Figure 1) and defined L as the radius of its inner circle. Laser severing was performed using Ti:Sapphire laser (Mai Tai DeepSee, Spectra Physics) in two-photon mode at 890 nm, < 100 fs pulses, 80 MHz repetition rate, ~ 0.2 W at the back focal plane, used at slightly less than full power to avoid cavitation (ESM Figure 2) [21]. Severing itself had a duration ranging from 217 to 1300 ms (according to the size of the region of interest and the scanning mode) during which no image was acquired. We could check that the severing had been effective to remove their adherens junctions, rather than simply bleach them (ESM Figure 2): after retraction the cells at the wound margin moved apart more than a cell diameter; moreover, there was no fluorescence recovery (Figure 1 (d)).

B. Analysis

At the tissue scale, for each frame after the severing the inner severed tissue boundary was fitted with an ellipse (Figure 1 (c-d)) using the ovsucle [36] ImageJ plugin [55]. We have modified it so that each fitting procedure started from the ellipse fitted on the preceding image: such tracking improved the speed and robustness. Data of Figure 2 are linearly fitted over a 5 frames sliding window in order to improve the signal to noise of position and velocity determinations.

Independently, at the cell scale, images were denoised with Safir software [56, 57]. We took the logarithm of the grey levels, to obtain comparable intensity gradients in differently contrasted parts of the image (Figure 4 (a)). This allowed us to use Kanade-Lucas-Tomasi (KLT) [58, 59] tracking algorithm [60] by selecting $\sim 10^2$ “features” of interest, corresponding to most cell vertices (Figure 4 (a)). Features were tracked from frame to frame: they followed the cell vertex movement towards the center, and we have observed no cell neighbour swapping. We checked that the features’ center of mass had only a small displacement, which we subtracted from individual feature displacements without loss of generality. To implement a quasi-1D analysis, we collected the features in a band along the Y axis and similarly along the X axis (Figure 4 (b-c)), and both axes were analysed separately. The band width (here 1/3 of the initial circle diameter) was chosen to be large enough to perform large statistics on features, and small enough to treat the features displacement as one-dimensional.

C. Comparison of model with experimental data

We numerically solved adimensionalized equations (see ESM) using the Matlab solver `pdepe`. For a given set of parameter values (τ, ξ) , we calculated ε_0 from the strain of the feature of largest initial amplitude, and rescaled the solution of ESM Equation 21 so as to satisfy ESM Equation 10. Using the experimental initial positions of features $\vec{R}_i^{\text{exp}}(t = 0^+)$ and the calculated strain field $\varepsilon(z, t)$, we simulated the trajectories $\vec{R}_i^{\text{sim}}(t)$, $i = 1 \dots N_f$, where N_f was the number of features.

The mismatch \mathcal{E} with our computation was evaluated by comparison with the experimental trajectories,

$$\vec{R}_i^{\text{exp}}(t):$$

$$\mathcal{E} = \frac{1}{N_f} \sum_{i=1}^{N_f} \frac{1}{t_\infty} \sum_{t=1}^{t_\infty} \|\vec{R}_i^{\text{sim}}(t) - \vec{R}_i^{\text{exp}}(t)\|^2, \quad (7)$$

where $\|\cdot\|$ denoted the Euclidean norm, and t_∞ the number of movie images.

ACKNOWLEDGMENTS

We gratefully thank F. Molino for modifying the ovucule plugin, P. Thévenaz and S. Birchfield for advices regarding their softwares, H. Oda for reagents, J.-M. Allain for suggesting to use KLT algorithm, lab members for discussions, and the PICT-IBiSA@BDD (UMR3215/U934) imaging facility of the Institut Curie. This work was supported by grants to Y.B. from ARC (4830), ANR (BLAN07-3-207540), ERC Starting Grant (CePoDro 209718), CNRS, INSERM, and Institut Curie; and by postdoc grants to I.B. by the FRM (SPF20080512397), to F.B. by the NWO (825.08.033).

-
- [1] Lecuit T, Lenne PF 2007 Cell surface mechanics and the control of cell shape, tissue patterns and morphogenesis. *Nat Rev Mol Cell Biol* 8:633–644.
- [2] Chen CS, Tan J, Tien J 2004 Mechanotransduction at cell-matrix and cell-cell contacts. *Annu Rev Biomed Eng* 6:275–302.
- [3] Ma X, Lynch HE, Scully PC, Hutson MS 2009 Probing embryonic tissue mechanics with laser hole drilling. *Phys Biol* 6:036004.
- [4] Lecuit T, Le Goff L 2007 Orchestrating size and shape during morphogenesis. *Nature* 450:189–192.
- [5] Mammoto T, Ingber DE 2010 Mechanical control of tissue and organ development. *Development* 137:1407–1420.
- [6] Fung YC 1993 *Biomechanics: mechanical properties of living tissues* (Springer).
- [7] Hufnagel L, Teleman AA, Rouault H, Cohen SM, Shraiman BI 2007 On the mechanism of wing size determination in fly development. *Proc Natl Acad Sci USA* 104:3835–3840.
- [8] Bittig T, Wartlick O, Kicheva A, Gonzalez-Gaitan M, Jülicher F 2008 Dynamics of anisotropic tissue growth. *New J Phys* 10:063001.
- [9] Blanchard G, *et al.* 2009 Tissue tectonics: morphogenetic strain rates, cell shape change and intercalation. *Nat Meth* 6:458–464.
- [10] Butler L, *et al.* 2009 Cell shape changes indicate a role for extrinsic tensile forces in *Drosophila* germ-band extension. *Nat Cell Biol* 11:859–864.
- [11] Ranft J, *et al.* 2010 Fluidization of tissues by cell division and apoptosis. *Proc Natl Acad Sci USA* 107:20863–20868.
- [12] Aigouy B, *et al.* 2010 Cell flow reorients the axis of planar polarity in the wing epithelium of *drosophila*. *Cell* 142:773–786.
- [13] Batchelor GK 2000 *An Introduction to Fluid Dynamics* (Cambridge University Press)
- [14] Ophir J, Cespedes I, Garra B, Ponnekanti H, Huang Y, Maklad N, 1996 Elastography: Ultrasonic imaging of tissue strain and elastic modulus in vivo *Eur J Ultrasound* 3:49–70.
- [15] Nienhaus U, Aegerter-Wilmsen T, Aegerter CM 2009 Determination of mechanical stress distribution in *drosophila* wing discs using photoelasticity. *Mech Dev* 126:942–949.
- [16] Desprat N, Supatto W, Pouille P, Beaupaire E, Farge E 2008 Tissue deformation modulates twist expression to determine anterior midgut differentiation in *drosophila* embryos. *Dev Cell* 15:470–477.
- [17] Fleury V, *et al.* 2010 Introducing the scanning air puff tonometer for biological studies. *Phys Rev E* 81:021920.
- [18] Peaucelle A, Braybrook S, Le Guillou L, Bron E, Kuhlemeier C, Höfte H, 2011 Pectin-induced changes in cell wall mechanics underlie organ initiation in *Arabidopsis*. *Curr Biol* 21:1720–1726.
- [19] Rauzi M, Lenne PF 2011 Cortical forces in cell shape changes and tissue morphogenesis. *Curr Top Dev Biol* 95:93–144.
- [20] Hutson MS, *et al.* 2003 Forces for morphogenesis investigated with laser microsurgery and quantitative modeling. *Science* 300:145–149.
- [21] Hutson MS, Ma X 2007 Plasma and cavitation dynamics during pulsed laser microsurgery in vivo. *Phys Rev Lett* 99:158104.
- [22] Hutson MS, *et al.* 2009 Combining laser microsurgery and finite element modeling to assess cell-level epithelial mechanics. *Biophys J* 97:3075–3085.
- [23] Kiehart DP, Galbraith CG, Edwards KA, Rickoll WL, Montague RA 2000 Multiple forces contribute to cell sheet morphogenesis for dorsal closure in *drosophila*. *J Cell Biol* 149:471–490.
- [24] Peralta XG, *et al.* 2007 Upregulation of forces and morphogenic asymmetries in dorsal closure during *drosophila*

- development. *Biophys J* 92:2583–2596.
- [25] Farhadifar R, Röper J, Aigouy B, Eaton S, Jülicher F 2007 The influence of cell mechanics, cell-cell interactions, and proliferation on epithelial packing. *Curr Biol* 17:2095–2104.
- [26] Rauzi M, Verant P, Lecuit T, Lenne PF 2008 Nature and anisotropy of cortical forces orienting drosophila tissue morphogenesis. *Nat Cell Biol* 10:1401–1410.
- [27] Landsberg KP, *et al.* 2009 Increased cell bond tension governs cell sorting at the drosophila anteroposterior compartment boundary. *Curr Biol* 19:1950–1955.
- [28] Fernandez-Gonzalez R, Simoes SdM, Röper J, Eaton S, Zallen JA 2009 Myosin II dynamics are regulated by tension in intercalating cells. *Dev Cell* 17:736–743.
- [29] Bosveld F, Bonnet I, Guirao B *et al.* 2012 Mechanical control of morphogenesis by Fat/Dachsous/Four-Jointed planar cell polarity pathway. *Science*, in press.
- [30] Mayer M, Depken M, Bois JS, Jülicher F, Grill SW 2010 Anisotropies in cortical tension reveal the physical basis of polarizing cortical flows. *Nature* 467:617–621.
- [31] Martin AC, Gelbart M, Fernandez-Gonzalez R, Kaschube M, Wieschaus EF 2010 Integration of contractile forces during tissue invagination. *J Cell Biol* 188:735–749.
- [32] Janiaud E, Graner F, 2005 Foam in a two-dimensional Couette shear: a local measurement of bubble deformation. *J Fluid Mech* 532:243–267.
- [33] Graner F, Dollet B, Raufaste C, Marmottant P 2008 Discrete rearranging disordered patterns, part i: robust statistical tools in two or three dimensions. *Eur Phys J E* 25:349–369.
- [34] Bainbridge SP, Bownes M 1981 Staging the metamorphosis of *Drosophila melanogaster*. *J Embryol exp Morph* 66:57-80
- [35] Langevin J, *et al.* 2005 *Drosophila* exocyst components sec5, sec6, and sec15 regulate DE-Cadherin trafficking from recycling endosomes to the plasma membrane. *Dev Cell* 9:365–376.
- [36] Thévenaz P, Delgado-Gonzalo R, Unser M 2011 The ovuscul. *IEEE Trans Pattern Anal Mach Intell* 33:382–393.
- [37] Hoger A, 1987 The stress conjugate to logarithmic strain. *Int J Solids Struct* 23:1645-1656.
- [38] Farahani K, Naghdabadi R, 2000 Conjugate stresses of the Seth-Hill strain tensors. *Int J Solids Struct* 37:5247-5255.
- [39] Tanner R, Tanner E 2003 Heinrich Hencky: a rheological pioneer. *Rheologica Acta* 42:93–101.
- [40] Wottawah F, *et al.* 2005 Optical rheology of biological cells. *Phys Rev Lett* 94:098103.
- [41] Marmottant P, *et al.* 2009 The role of fluctuations and stress on the effective viscosity of cell aggregates. *Proc Natl Acad Sci USA* 106:17271–17275.
- [42] Guevorkian K, Gonzalez-Rodriguez D, Carlier C, Dufour S, Brochard-Wyart F 2011 Mechanosensitive shivering of model tissues under controlled aspiration. *Proc Natl Acad Sci USA* 108:13387–13392.
- [43] Guevorkian K, Colbert M, Durth M, Dufour S, Brochard-Wyart F 2010 Aspiration of biological viscoelastic drops. *Phys Rev Lett* 104:218101.
- [44] Flanagan MD, Lin S 1980 Cytochalasins block actin filament elongation by binding to high affinity sites associated with F-actin. *J Biol Chem* 255:835-838.
- [45] Nolen BJ, Tomasevic N, Russell A, Pierce DW, Jia Z, McCormick CD, Hartman J, Sakowicz R, Pollard TD 2009 Characterization of two classes of small molecule inhibitors of Arp2/3 complex. *Nature* 460:1031-1034.
- [46] Uehata M, Ishizaki T, Satoh H, Ono T, Kawahara T, Morishita T, Tamakawa H, Yamagami K, Inui J, Maekawa M, Narumiya S. 1997 Calcium sensitization of smooth muscle mediated by a Rho-associated protein kinase in hypertension. *Nature* 389:990-994.
- [47] Papusheva E, Heisenberg CP 2010 Spatial organization of adhesion: force-dependent regulation and function in tissue morphogenesis. *EMBO J*. 29:2753-2768.
- [48] Brodland GW, *et al.* 2010 Video force microscopy reveals the mechanics of ventral furrow invagination in *Drosophila*. *Proc Natl Acad Sci USA* 107:22111–22116.
- [49] MacKintosh F, Schmidt C 1999 Microrheology. *Curr Opinion Coll Interface Science* 4:300-307.
- [50] Panorchan P, Lee JSH, Daniels BR, Kole TP, Tseng Y, Wirtz D, 2007 Probing cellular mechanical responses to stimuli using ballistic intracellular nanorheology. *Methods Cell Biol* 83:115-140
- [51] Crocker JC, Hoffman BD 2007 Multiple-particle tracking and two-point microrheology in cells. *Methods Cell Biol* 83:141–178.
- [52] Roberts DB 1998 *Drosophila: A Practical Approach* (Oxford University Press, USA), 2 edition.
- [53] Ségalen M, *et al.* 2010 The Fz-Dsh planar cell polarity pathway induces oriented cell division via Mud/NuMA in *drosophila* and zebrafish. *Dev Cell* 19:740–752.
- [54] Oda H, Tsukita S 2001 Real-time imaging of cell-cell adherens junctions reveals that *drosophila* mesoderm invagination begins with two phases of apical constriction of cells. *J Cell Sci* 114:493–501.
- [55] Ovuscul. <http://bigwww.epfl.ch/thevenaz/ovuscul/>.
- [56] Kervrann C, Boulanger J 2006 Optimal spatial adaptation for patch-based image denoising. *IEEE Trans Image Process* 15:2866–2878.
- [57] Boulanger J, *et al.* 2010 Patch-based nonlocal functional for denoising fluorescence microscopy image sequences. *IEEE Trans Med Imaging* 29:442–454.
- [58] Lucas B, Kanade T 1981 An iterative image registration technique with an application to stereo vision. *International Joint Conference on Artificial Intelligence* pp 674–679.
- [59] Tomasi C, Kanade T 1991 Detection and tracking of point features. *Carnegie Mellon University Technical Report* CMU-CS-91-132.
- [60] KLT: Kanade-Lucas-Tomasi feature tracker. <http://www.ces.clemson.edu/~stb/klt/>.

Electronic Supplementary Material (ESM)

MODEL

The external dissipation is not accessible to single cell junction ablation experiments and its estimate requires modelling [1]. Our model is analogous to models of viscoelastic relaxation proposed for local severing experiments of acto-myosin bundles in living cells [2].

Hypotheses

We use an Eulerian description. Since the severed domain area visibly decreases with time, we do not enforce any in-plane incompressibility condition. Note also that in-plane incompressibility would fix the velocity profile, which is incompatible with the experimental observation of different profiles (Figure 5). We rather assume for simplicity that the out-of-plane thickness is a passive variable: hence the 3D Poisson ratio is 1/2, but the in-plane effective 2D Poisson ratio vanishes. We test this hypothesis by checking *a posteriori* that the model predictions are compatible with experimental observations. Within this simplification, the antero-posterior X and medio-lateral Y axes (Figure 1) then decouple. Finally, we define σ as the part of stress which has been removed by ablation.

We thus consider only one spatial dimension, with the variable z denoting position along either X or Y . We model the retracting slab of tissue as a linear viscoelastic Kelvin-Voigt material (that is, with a steady response at long time) with a Young modulus E and a viscosity η . We neglect the line tension around the tissue domain: first, because we observe that the ellipse does not remain round (this suggests the line tension is weak, without being a proof, since we could also imagine that it has the same anisotropy as the strain); second, because even if the line tension exists, it is small enough that the ellipse contour remains visibly rough, see Movies 1-3. Two terms contribute explicitly to σ : an elastic one (which implicitly includes the external pressure) and a viscous one:

$$\sigma(z, t) = E \varepsilon(z, t) + \eta \frac{\partial v}{\partial z}(z, t). \quad (8)$$

Taking into account a fluid external friction, with a friction coefficient ζ of dimension Pa.s.m⁻², the force balance equation reads:

$$\frac{\partial \sigma}{\partial z}(z, t) - \zeta v(z, t) = 0. \quad (9)$$

Combining Equations 3, 8 and 9 yields Equation 4.

Initial, boundary and final conditions

The initial length of the retracting slab is $2L$: $z \in [-L, L]$. Assuming that the initial state respects mechanical equilibrium (over the relevant time scale of 10 to 100 s), the initial strain is uniform, and we have for all z :

$$\begin{aligned} \varepsilon(z, t = 0) &= \varepsilon_0, \\ \sigma(z, t = 0) &= E\varepsilon_0. \end{aligned} \quad (10)$$

At the boundary of the severed region, we have for all t :

$$\sigma(\pm L, t) = 0. \quad (11)$$

Since the final state is at mechanical equilibrium, we have for all z :

$$\begin{aligned} \lim_{t \rightarrow \infty} \varepsilon(z, t) &= 0, \\ \lim_{t \rightarrow \infty} \sigma(z, t) &= 0. \end{aligned} \quad (12)$$

Injecting Equation 3 into Equation 8, using conditions given by Equations 10-12 yields by integration over time:

$$\varepsilon(\pm L, t) = \varepsilon_0 e^{-t/\tau}, \quad (13)$$

where the relaxation time is viscoelastic: $\tau = \frac{\eta}{E}$.

Initial velocity profile

Equations 3, 10, 13 yield an approximate analytical prediction for the initial velocity profile at time $\delta t \ll \tau$, as follows. An expansion of ε at first order in $\frac{\delta t}{\tau}$:

$$\varepsilon(z, \delta t) = \varepsilon_0 + \varepsilon_1(z) \frac{\delta t}{\tau}, \quad (14)$$

defines the initial strain rate as:

$$\frac{\varepsilon_1(z)}{\tau} = \frac{\varepsilon(z, \delta t) - \varepsilon_0}{\delta t} \approx \frac{\partial \varepsilon}{\partial t}(z, t = 0). \quad (15)$$

Substituting Equations 14-15 into Equation 4, we obtain an ordinary differential equation for $\varepsilon_1(z)$:

$$D\tau \frac{d^2 \varepsilon_1}{dz^2} - \varepsilon_1(z) = 0, \quad (16)$$

with a diffusion coefficient $D = \frac{E}{\zeta}$. With the boundary condition $\varepsilon_1(z = \pm L) = -\varepsilon_0$, the solution of Equation 16 reads:

$$\varepsilon_1(z) = -\varepsilon_0 \frac{\cosh kz}{\cosh kL} \quad (17)$$

where $k^2 = \frac{1}{D\tau}$, or $kL = \xi^{1/2}$ since $\xi = \frac{\zeta L^2}{\eta}$. Spatial integration of Equation 17 using Equations 3 and 15 yields Equation 6.

Limit regimes

ESM Figure 4 shows two limit regimes of Equation 4.

- When internal viscosity dominates: external friction may be neglected, and Equation 9 reduces to $\frac{\partial \sigma}{\partial z} = 0$, so that σ is uniform and its value is fixed at the boundaries: $\sigma(z, t) = \sigma(\pm L, t) = 0$ for all (z, t) . Integration yields:

$$\varepsilon(z, t) = \varepsilon_0 e^{-t/\tau}. \quad (18)$$

The strain is uniform at all times (ESM Figure 4 (A)). Since the center of the slab does not move, $v(0, t) = 0$ for all t , the velocity profile is linear:

$$v(z, t) = \int_0^z \frac{\partial \varepsilon}{\partial t}(z', t) dz' = -\frac{\varepsilon_0}{\tau} z e^{-t/\tau}. \quad (19)$$

As expected, in the limit of small friction $\xi \ll 1$, Equation 6 reduces to Equation 19 when $t = 0$. In this regime, all parts of the tissue relax exponentially with the same time scale τ .

- When external friction dominates: the internal viscosity of the tissue may be neglected. Combining Equations 3, 8 and 9 yields a diffusion equation for the strain field:

$$\frac{\partial \varepsilon}{\partial t} = D \frac{\partial^2 \varepsilon}{\partial z^2} \quad (20)$$

with conditions given by Equations 10-12. Strain diffuses from the boundaries on a time scale $\tau_D = L^2/D = \zeta L^2/E$, and the strain field remains inhomogeneous until $t \gg \tau_D$ (ESM Figure 4 (B)).

One may note that the strain diffusion equation (Equation 20) is identical to that obtained in the context of gel dynamics [3, 4]. Taking into account interstitial flow (*i.e.* the transport of water across the epithelium) would only modify the diffusion constant: $D_{\text{permeation}} = E \left(\frac{1}{\kappa} + \zeta \right)^{-1}$, where κ is the permeability coefficient.

Dimensionless variables

In the general case, to solve Equation 4 numerically we normalize variables by defining: $\bar{z} = z/L$, $\bar{t} = t/\tau$ and $\bar{\varepsilon} = \varepsilon/\varepsilon_0$. Equation 4 then becomes:

$$\xi \frac{\partial \bar{\varepsilon}}{\partial \bar{t}} = \frac{\partial^2 \bar{\varepsilon}}{\partial \bar{z}^2} + \frac{\partial^3 \bar{\varepsilon}}{\partial \bar{t} \partial \bar{z}^2} \quad (21)$$

with the initial condition:

$$\bar{\varepsilon}(\bar{z}, \bar{t} = 0) = 1, \quad (22)$$

the boundary conditions:

$$\bar{\varepsilon}(\bar{z} = \pm 1, \bar{t}) = e^{-\bar{t}}, \quad (23)$$

and the final conditions:

$$\bar{\varepsilon}(\bar{z}, \bar{t} \rightarrow \infty) = 0, \quad (24)$$

Since $\xi = \tau_D/\tau$, the limit regimes are recovered when $\tau_D \ll \tau$ (internal viscosity dominates, $\xi \ll 1$), and $\tau_D \gg \tau$ (external friction dominates, $\xi \gg 1$).

-
- [1] Mayer M, Depken M, Bois JS, Jülicher F, Grill SW 2010 Anisotropies in cortical tension reveal the physical basis of polarizing cortical flows. *Nature* 467:617–621.
- [2] Colombelli J, et al. 2009 Mechanosensing in actin stress fibers revealed by a close correlation between force and protein localization. *J Cell Sci* 122:1665–1679.
- [3] Charras GT, Mitchison TJ, Mahadevan L 2009 Animal cell hydraulics. *J Cell Sci* 122:3233–3241.
- [4] Doi M 2009 Gel dynamics. *J Phys Soc Jpn* 78:052001.

ESM FIGURES

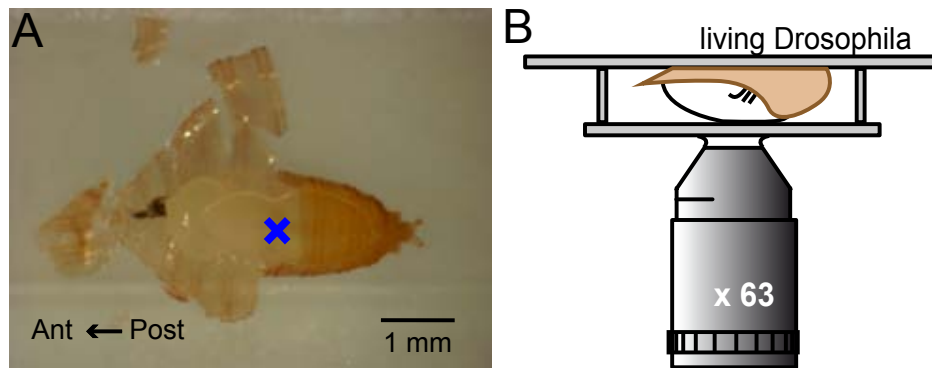


FIG. 1. (ESM) Set-up for live imaging. (A) The pupal case (light brown) is partially removed, while the cuticle (transparent) is kept intact. Blue cross: approximate position of severing, along the symmetry axis of the scutellum. (B) The pupa (white) is mounted between slide and coverslip with its back facing the objective (dark grey). Antero-posterior axis is horizontal (anterior towards the left, posterior towards the right).

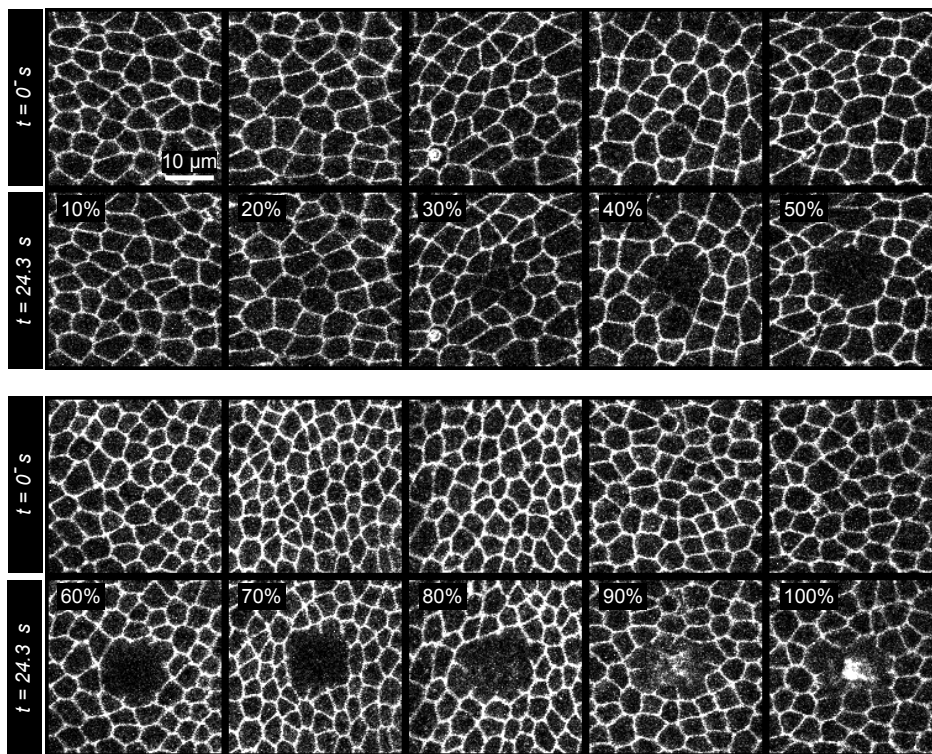


FIG. 2. (ESM) Range of acceptable severing powers. Images shown are just before the severing (top) and 24.3 s after the severing (bottom) as a function of the proportion (indicated at top left) of the full laser power, here at 890 nm. Below 20%, no severing occurs. From 30 to 50%, severing is partial. From 60 to 80%, severing is complete and cell-cell junctions move significantly; experiments presented in this work are performed in this range. Above 90%, cavitation occurs. These ranges vary slightly from one experiment to the other, so that the quality of severing must be carefully assessed *a posteriori*.

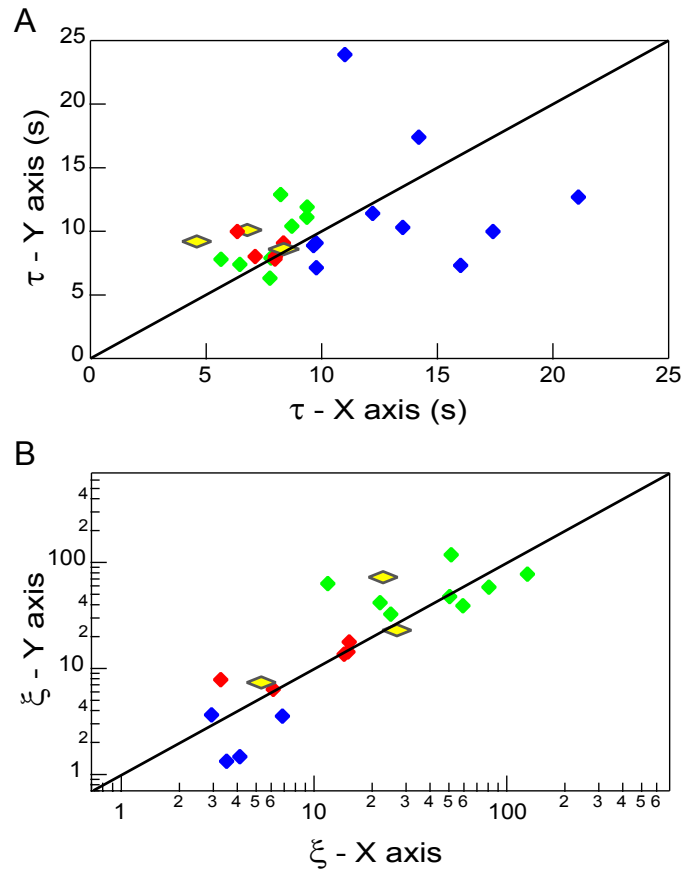


FIG. 3. (ESM) Check of τ and ξ isotropy. (A) Relaxation time τ : for each experiment, represented by one point, we plot the value obtained along the Y direction (estimated as in the Inset of Figure 2) *versus* the value obtained along the X direction. Age is color-coded as in Figure 3: green, young; red, middle-aged; blue, old. (B) Same plot for the friction/viscosity ratio ξ , fitted by Equation 6 as in Figure 5. Note the logarithmic scale. Two values of ξ of order 10^{-3} and 10^{-4} are below the plotted range.

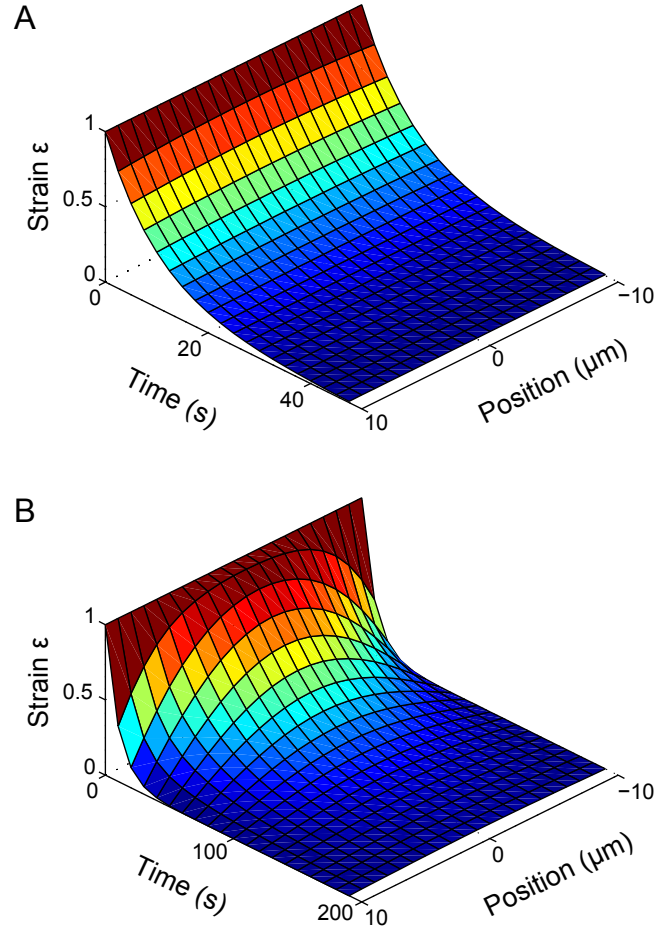


FIG. 4. (ESM) Limit regimes: space-time profiles of strain fields obtained from numerical simulations of Equation 4 for $\epsilon_0 = 1$, $\tau = 10$ s, $L = 10$ μm . (A) Uniform strain relaxation, when internal viscosity dominates (low ξ , initial velocity profile similar to the blue curve in Figure 5): $D = 100$ $\mu\text{m}^2.\text{s}^{-1}$, $\tau_D = 1$ s. (B) Strain diffusion, when external friction dominates (high ξ , initial velocity profile similar to the green curve in Figure 5): $D = 1$ $\mu\text{m}^2.\text{s}^{-1}$, $\tau_D = 100$ s. Strain value in each grid square is color-coded from 0 (dark blue) to 1 (dark red).

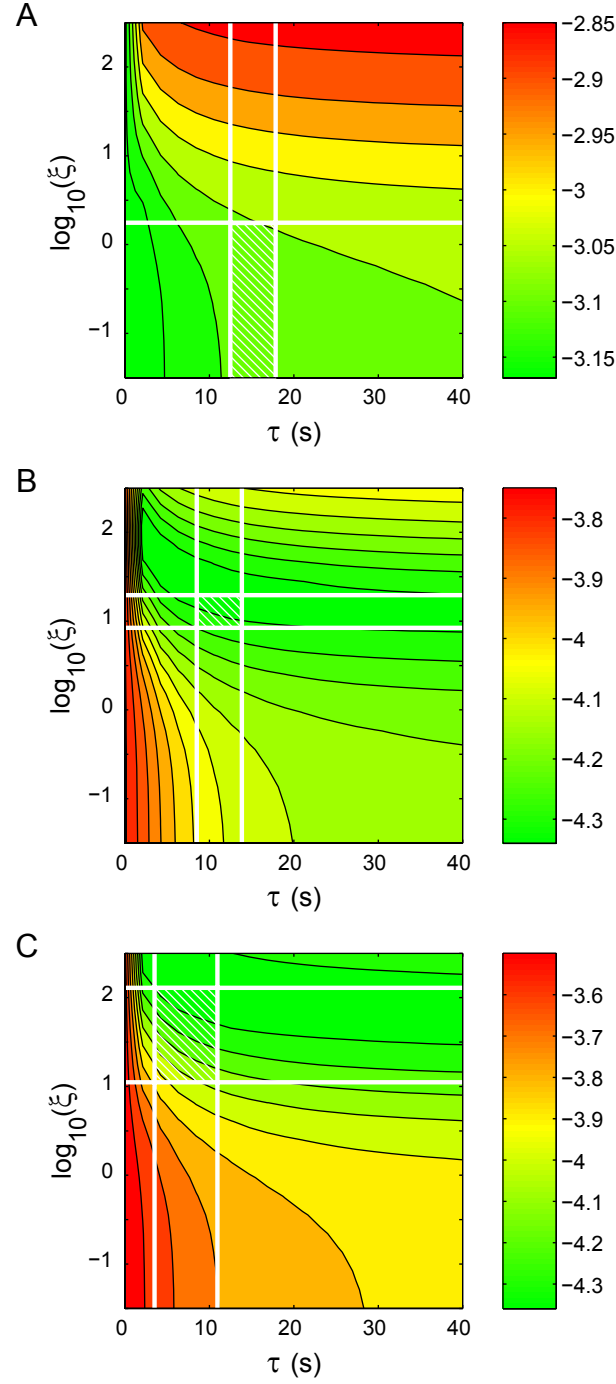


FIG. 5. (ESM) Error maps in the (τ, ξ) plane, semi-log axes. Experiments are those of Figure 5 and Movies 1-3; error is estimated according to Equation 7. The minimal region of the error landscape (its deepest valley) is too wide to allow a direct measurement of the parameters. However, depending on the orientation of the minimal region of the error landscape, the computed error maps fall broadly into three categories, which agree with the three age groups. There is also a good agreement with hatched regions, which are the results of the independent measurements of the parameters τ and ξ (Figure 3 (c) and ESM Figure 3). (A) Small ξ , old pupa (Movie 3). Minimal valley parallel to the ξ axis: this suggests that only an upper bound, of the order of 1 (white bar), can be given for the value of ξ . Friction is negligible. (B) Finite ξ , middle-aged pupa (Movie 2). Minimal valley intermediate, parallel to the τ axis: friction cannot be neglected, and ξ admits a finite estimate. (C) Large ξ , young pupa (Movie 1). Minimal valley parallel to the τ axis, at very large ξ : this suggests that only a lower bound can be given for the values of τ and ξ .